




# High-Resolution Simulation of the Near-Field Pollutant Dispersion in a Nuclear Power Plant Community with High-Performance Computing

Bowen Tang<sup>1,2</sup> · Hao Wang<sup>1</sup> · Jianjun Xu<sup>1</sup> · Jiazhen Lin<sup>1</sup> · Jinxing Hu<sup>2</sup> · Rongliang Chen<sup>2,3</sup> 

Received: 14 November 2023 / Accepted: 9 January 2024  
© The Author(s) 2024

## Abstract

This study aims to employ numerical simulations to understand the dynamics of wind fields and air pollutant dispersion in the proximity of a nuclear plant, situated within a specified urban environment. By leveraging computational fluid dynamics (CFD) combined with geographical information system (GIS) data, the research comprehensively models atmospheric interactions in terms of wind flow patterns, building-induced pressure variances, and pollutant trajectories. The computational domain extends over an area of  $8.8 \text{ km} \times 8.4 \text{ km}$ , vertically stretching to  $0.5 \text{ km}$ . The wind and pollutant distribution equations are discretized using the finite volume method, providing detailed insights into fluid interactions with urban topographies. Key findings highlight the profound influences of terrain, urban structures, and wind flow behavior on the dispersion of radioactive aerosols, shedding light on potential risks and safety protocols for nuclear plant environments.

**Keywords** Computational Fluid dynamics · Parallel computing · Finite volume method · Air pollutant distribution

---

✉ Jinxing Hu  
jinxing.hu@siat.ac.cn

✉ Rongliang Chen  
rl.chen@siat.ac.cn

<sup>1</sup> State Key Laboratory of Nuclear Power Safety Technology and Equipment, China Nuclear Power Engineering Co., Ltd., Shenzhen 518172, Guangdong, China

<sup>2</sup> Shenzhen Institute of Advanced Technology, Chinese Academy of Sciences, Shenzhen 518055, Guangdong, China

<sup>3</sup> Shenzhen Key Laboratory for Exascale Engineering and Scientific Computing, Shenzhen 518055, Guangdong, China

## 1 Introduction

In recent years, the role of nuclear power plants has significantly evolved, emerging as a vital energy source in numerous countries, boasting the capability to generate substantial electricity while keeping greenhouse gas emissions to a minimum. However, the safe operation of these nuclear power facilities remains a matter of paramount concern, given the potential hazards associated with accidents and incidents that may culminate in the release of radioactive materials into the environment. In the unfortunate event of such a radioactive leakage, it is imperative to gain a profound understanding of the intricate behaviors exhibited by these materials within the ecosystem, encompassing their dispersion trajectory and transportation through the air.

Computational Fluid Dynamics (CFD), a sophisticated scientific tool that has been extensively harnessed for the purpose of simulating and analyzing fluid flow and transport phenomena. The allure of CFD models lies in their ability to precisely predict the behavior of fluid flows and the attendant transport processes, even within intricate and diverse geometries, under a spectrum of varying conditions [1]. Such capabilities render CFD an indispensable instrument for forecasting the dispersion and subsequent transport of pollutants in the environment, particularly in the vicinity of nuclear power plants.

Accurately predicting the dispersion of pollutants is challenging due to the intricate interplay between atmospheric currents and the flow patterns around structures. Pollutants introduced into the atmosphere from various sources disperse through a broad spectrum of horizontal length scales, categorized as far-field and near-field phenomena. In the far-field phenomena, horizontal air movement dominates over vertical motion, and the influence of individual buildings on pollutant dispersion becomes relatively minor. This aspect is primarily discussed concerning public health regulations related to air quality in urban environments [2]. On the other hand, near-field pollutant dispersion involves the interaction between the pollutant plume and the surrounding airflow, which can be altered by the presence of buildings. Consequently, it is crucial to consider this aspect when assessing both outdoor and indoor air quality, encompassing pollutant concentrations in the nearby streets and on building surfaces.

Recent advancements in computational science and precision measurement techniques have significantly enhanced our capacity to provide a comprehensive portrayal of the near-field pollution simulation within authentic urban landscapes. Within these complex urban environments, a rich tapestry of coexisting turbulence structures unfolds, resulting in an intricate velocity energy spectrum that spans the entire range, extending from the smallest viscosity scales to the larger integral length scales. These developments allow us to delve deeper into the dynamics of the near-field pollution dispersion, facilitating a detailed understanding of how urban morphology interacts with the various turbulence structures present. This refined analysis empowers us to capture the full spectrum of velocity energy, encompassing the minute-scale interactions near the viscosity range and extending seamlessly to the broader patterns defined by integral length scales.

A plethora of studies have explored near-field pollution simulation via Computational Fluid Dynamics (CFD), with many harnessing the Reynolds-averaged Navier–Stokes (RANS) approach as a foundational technique (Wen et al. [3], Most, 2021 [4], Md Eabad [5]). Over the past few decades, there has been a discernible pivot towards the application of large-eddy simulation (LES) due to its superior capacity to resolve large-scale unsteady motions. This shift allows for the capture of the highly dynamic nature of wind velocity and pollutant concentration within urban street canyons, thus markedly enhancing simulation accuracy (Zheng [6], Tominaga et al. [1]).

Pioneering applications of LES include the work of Letzel et al. [7], who employed the parallelized LES model PALM to probe pedestrian-level ventilation in densely populated areas of Kowloon, Hong Kong. The call for standardized wind comfort assessment procedures was echoed by Janssen et al. [8] through a demonstrative CFD-based case study. In parallel, Montazeri et al. [9] appraised a novel facade design via 3D RANS simulations aimed at reducing wind speeds around Antwerp’s Park Tower.

Further advancements were made when Onodera [10] devised a CFD code based on the Lattice Boltzmann Method (LBM), paving the way for extensive urban-scale simulations. Shi et al. [11] employed this approach in their examination of an urban development near Lake Tai, China, showcasing the practicality of assessment methodologies. LES was further refined by Ikeda et al. [12], who developed a model adept at assessing the impact of urban features, like buildings and vegetation, on local temperature distributions.

In a combined approach, Zheng et al. [13] integrated wind tunnel experiments with CFD simulations to study the pedestrian-level wind environment, underscoring the symbiotic relationship between empirical data and simulation for environmental assessments. Each of these studies contributes to a more nuanced and sophisticated understanding of urban wind environments, illustrating the evolution and application of CFD techniques in real-world scenarios.

In recent advancements within the realm of urban flow simulations, several studies stand out. Jacob et al. [14] employed Large-Eddy Simulation (LES) rooted in the Lattice Boltzmann Method (LBM) to assess flows in a full-scale urban model. Their study specifically sought to juxtapose various wind comfort criteria, thereby providing benchmarks for urban design. In a complementary approach, Sousa et al. [15] introduced a validation study which leveraged a Bayesian inference method. Their focus was to estimate inflow boundary conditions for Reynolds-averaged Navier–Stokes (RANS) simulations. By assimilating data gleaned from urban sensors, they enhanced the precision of urban flow simulations.

Building on these studies, Liu et al. [16] embarked on a nuanced exploration to delineate the contributions of different eddy types within the Atmospheric Surface Layer, especially above dense urban landscapes. Their research aims to furnish critical insights for urban planners, spotlighting methodologies to amplify both ventilation and the effective dispersion of pollutants, ensuring healthier urban environments.

This paper undertakes the commendable endeavor of presenting a comprehensive CFD simulation study that delves into the dispersion and transportation dynamics of

pollutants emanating from a hypothetical nuclear power plant operating under the influence of complex wind conditions. The primary aim of this study is to scrutinize the multifaceted impacts brought about by wind turbulence, thermal stability, and intricate topographical features on the dispersion and subsequent transport of pollutants. The intrinsic significance of this research lies in its potential to provide indispensable insights for enhancing safety protocols and emergency response planning for nuclear power plants. The resulting data can be utilized to pinpoint potential areas of concern and, in turn, refine the design of emergency response strategies. Furthermore, this study offers a unique opportunity to glean insights into the potential repercussions of a nuclear power plant accident on the environment and the health of the public.

Compared to prior research [17–20] on pollutant dispersion and transport, our study stands out due to its extensive modeling approach. We utilize a comprehensive model spanning 64 km<sup>2</sup>, which meticulously incorporates topographical complexities like hills, valleys, and urban structures. These features significantly affect wind and pollutant dispersion patterns. The expansive scope and attention to detailed topography make our study not only more realistic but also highly relevant to real-world applications.

To conclude, this paper unfolds a remarkable CFD simulation study, one that meticulously examines the dispersion and transportation dynamics of pollutants emanating from a hypothetical nuclear power plant under the sway of complex wind conditions. The knowledge gleaned from this study carries the potential to fundamentally enhance the safety and emergency response planning for nuclear power plants, while concurrently shedding light on the potential environmental and public health consequences of a nuclear power plant accident. By harnessing a large-scale complex model teeming with realistic topographical features, our study furnishes a comprehensive and practical analysis of pollutant dispersion and transport that can be directly translated to real-world scenarios. The method developed in this paper can be used for some inverse problem study, and we refer to [21–26] for some recent important progress on related studies.

## 2 Methodology

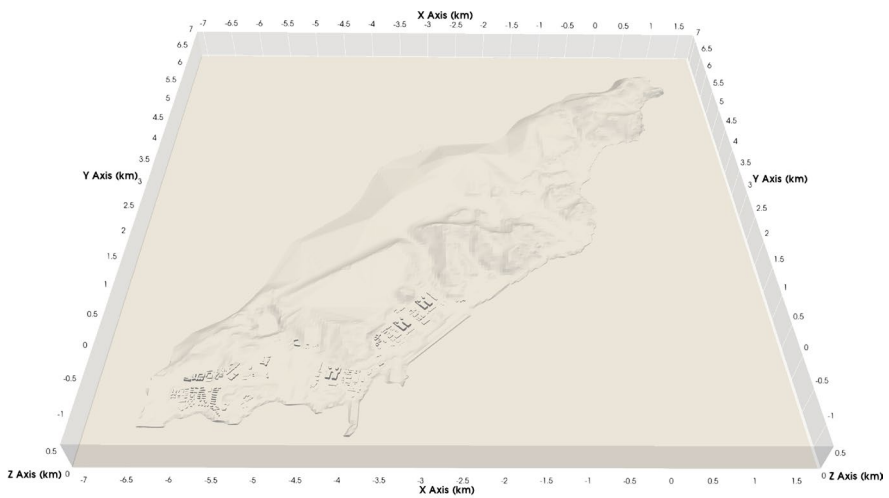
The numerical simulation of the wind and air pollution employs computational models and algorithms to replicate and analyze the intricate interplay between atmospheric conditions, urban topography, and pollutant sources. Through advanced numerical simulations, researchers and environmental experts can gain critical insights into air quality, pollutant distribution, and the effectiveness of mitigation strategies. In this section, we will outline the key components and approaches that constitute the methodology for numerical simulation of the wind and air pollution.

### 2.1 Computational Domain

A robust geospatial foundation is pivotal for the precise simulation of airflow patterns, pollutant dispersion, and their interactions within urban environments. This

study zeroes in on a specific neighborhood surrounding a nuclear plant, encompassing an area of  $8.8 \text{ km} \times 8.4 \text{ km}$ , as illustrated in Fig. 1.

The simulation relies on geographic information system (GIS) data for the geometry, topographical details, and building models [27]. GIS outlines building projections onto the floor using single or multiple polygons, either convex or concave. Coupled with the building's height data, we produce a 3D model. Each polygon side becomes a rectangular face of the building, which is then triangulated and saved as an stereolithography (STL) format for flow simulation. The simulation spans a horizontal area of  $8.8 \text{ km} \times 8.4 \text{ km}$  and extends vertically to  $0.5 \text{ km}$ , resulting in a computational domain of  $8.8 \times 8.4 \times 0.5 \text{ km}^3$ , illustrated in Fig. 1a. This domain contains 213 structures, with three main nuclear facilities detailed in Fig. 1b.



(a) An overview the topography for the nuclear power plant site.



(b) An overview of the building layout within the nuclear power plant site.

**Fig. 1** **a** An overview of the topography and **b** building distribution for the nuclear power plant site. The computational volume encompasses dimensions of  $8.8 \times 8.4 \times 0.5 \text{ km}^3$ . Three primary nuclear facilities are highlighted using red numbers. Of particular interest in our study is the facility in the top right, marked by red 3, which is the source of the pollutant leak

The computational domain encompasses both the inlet and outlet sides, determined by the wind field direction. With an initial grid resolution set at 50 m per cell, the total mesh count stands at  $180 \times 170 \times 14 = 428,400$ . Given the relative smallness of individual buildings in comparison to the entire domain, refinement regions are introduced. This allows for a higher-resolution mesh, specifically refining areas within a 4-m distance from the building surfaces. As a result, the final total mesh count is approximately 15 million.

## 2.2 Governing Equations

In this section, we present the fundamental governing equations that form the basis of our numerical simulation model for air pollution distribution in the urban environment. The core equations are the Navier-Stokes equations for fluid flow and the transport equation for pollutant dispersion.

### 2.2.1 Navier–Stokes Equations

The Navier–Stokes equations describe the conservation of momentum in fluid flow. In a three-dimensional Cartesian coordinate system, they can be written as [28, 29]:

$$\frac{\partial \mathbf{u}}{\partial t} + (\mathbf{u} \cdot \nabla) \mathbf{u} = -\frac{1}{\rho} \nabla p + \nu \nabla^2 \mathbf{u} + \mathbf{f} \quad (1)$$

Where:

$\mathbf{u} = (u, v, w)$  is the fluid velocity vector.

$t$  is time.

$\rho$  is the fluid density.

$p$  is the pressure.

$\nu$  is the kinematic viscosity.

$\mathbf{f}$  represents external forces (e.g., gravity).

The continuity equation for mass conservation is given by:

$$\nabla \cdot \mathbf{u} = 0 \quad (2)$$

### 2.2.2 Transport Equation for Pollutant Dispersion

To simulate the dispersion of pollutants (e.g.,  $C$  for pollutant concentration), we use the advection–diffusion equation:

$$\frac{\partial C}{\partial t} + \mathbf{u} \cdot \nabla C = D \nabla^2 C + S, \quad (3)$$

where  $D$  is the diffusion coefficient of the pollutant.  $S$  represents pollutant sources or sinks (e.g., emissions from the nuclear facilities).

### 2.2.3 Turbulence Modeling

To accurately simulate turbulence, we require a turbulence model. In this study, we employ the  $k - \omega$  Shear Stress Transport (SST) turbulence model, as outlined by Menter [30]. This model has proven effective for turbulent flow simulations, as demonstrated by Toparlak et al. [31]. The  $k - \omega$  SST model, a two-equation eddy-viscosity model, is governed by the following equations [30].

$$\begin{aligned} \rho \frac{\partial \omega}{\partial t} + \rho(\vec{v} \cdot \nabla)\omega &= -\rho\beta\omega^2 + \nabla \cdot [(\mu + \sigma_\omega\mu_t)\nabla\omega] \\ &+ \gamma\rho\{[(\nabla \otimes \vec{v}) + (\nabla \otimes \vec{v})^T] : (\nabla \otimes \vec{v})\} \\ &+ 2\rho(1 - F_1)\sigma_{\omega 2}\frac{1}{\omega}\nabla k \cdot \nabla\omega, \end{aligned} \tag{4}$$

$$\begin{aligned} \rho \frac{\partial k}{\partial t} + \rho(\vec{v} \cdot \nabla)k &= \nabla \cdot [(\mu + \sigma_k\mu_t)\nabla k] \\ &+ \tilde{P}_k - \rho\beta^*\omega k. \end{aligned}$$

In these equations,  $k$  represents the turbulence kinetic energy and  $\omega$  denotes the specific rate of dissipation. The term  $\tilde{P}_k$  indicates the effective rate of production of  $k$ . The model’s diffusion coefficients are represented by  $\sigma_k$  and  $\sigma_\omega$ . The turbulence modeling constants include  $\sigma_{\omega 1}$ ,  $\sigma_{\omega 2}$ ,  $\gamma_1$ ,  $\gamma_2$ ,  $\beta_1$ ,  $\beta_2$  and  $\beta^*$ . Both  $\beta$  and  $\gamma$  determined by Menter’s blending function, which is provided as follows:

$$\begin{aligned} \beta &= \beta_1 F_1 + \beta_2(1 - F_1), \\ \gamma &= \gamma_1 F_1 + \gamma_2(1 - F_1), \end{aligned} \tag{5}$$

$\gamma_1$  and  $\gamma_2$  is given by

$$\begin{aligned} \gamma_1 &= \beta_1/\beta^* - \sigma_{\omega 1}\kappa^2/\sqrt{(\beta^*)}, \\ \gamma_2 &= \beta_2/\beta^* - \sigma_{\omega 2}\kappa^2/\sqrt{(\beta^*)}, \end{aligned} \tag{6}$$

where  $\kappa$  represents the von Kármán constant. Both  $\sigma_k$  and  $\sigma_\omega$  are determined by Menter’s blending function, as follows:

$$\begin{aligned} \sigma_k &= \sigma_{k1}F_1 + \sigma_{k2}(1 - F_1), \\ \sigma_\omega &= \sigma_{\omega 1}F_1 + \sigma_{\omega 2}(1 - F_1). \end{aligned} \tag{7}$$

The Menter’s first blending function  $F_1$  is defined as

$$F_1 = \tanh\left\{ \left[ \min \left[ \max \left( \frac{\sqrt{k}}{\beta^*\omega y}, \frac{500\nu_t}{y^2\omega} \right), \frac{4\rho\sigma_{\omega 2}k}{CD_{k\omega}y^2} \right] \right]^4 \right\}, \tag{8}$$

where  $\nu_t$  is the kinematic viscosity, and the positive portion of cross-diffusion term  $CD_{k\omega}$  is defined as:

$$CD_{k\omega} = \max\left\{2\rho\sigma_{\omega 2}\frac{1}{\omega}\nabla k\nabla\omega, 10^{-10}\right\}. \quad (9)$$

Here  $y$  is the distance to the nearest wall. The operators “ $\otimes$ ” and “ $\cdot$ ” represent the dyadic product and the double-dot product (equivalent to the Frobenius inner product), respectively.  $\mu_t$  defines the scalar dynamic eddy viscosity coefficient, given by:

$$\mu_t = \rho\nu_t = \rho\frac{a_1k}{\max(a_1\omega, |\Omega|F_2)}, \quad (10)$$

where  $a_1$  represents a modeling constant, while  $F_2$  corresponds to the second blending function proposed by Menter, described as

$$F_2 = \tanh\left(\max\left(\frac{2\sqrt{k}}{\beta^*\omega y}, \frac{500\nu_t}{\omega y^2}\right)^2\right), \quad (11)$$

and  $|\Omega|$  is the absolute value of the mean vorticity vector defined as

$$|\Omega| = \sqrt{\left(\frac{\partial v_3}{\partial x_2} - \frac{\partial v_2}{\partial x_3}\right)^2 + \left(\frac{\partial v_1}{\partial x_3} - \frac{\partial v_3}{\partial x_1}\right)^2 + \left(\frac{\partial v_2}{\partial x_1} - \frac{\partial v_1}{\partial x_2}\right)^2}. \quad (12)$$

The coefficients appearing in equations (4)–(11) are shown in Table 1.

These equations govern the behavior of turbulence within the urban atmosphere and are coupled with the Navier–Stokes and pollutant transport equations to capture the turbulent dispersion of pollutants.

## 2.3 Numerical Methods

### 2.3.1 Spatial Discretization

To discretize the governing equations and solve them numerically, we employ the Finite Volume Methods (FVM). A hallmark of computational fluid dynamics (CFD), FVM is revered for its ability to provide accurate solutions to complex partial differential equations by ensuring local conservation of physical quantities such as mass, momentum, and energy.

The crux of the FVM lies in the manner it treats the computational domain. For effective FVM discretization, the domain is covered with a grid, often referred to as a mesh. This mesh is essentially a collection of small control volumes wherein the governing equations are applied. In the context of our simulations involving the urban

**Table 1** The value of the coefficients in the  $k - \omega SST$  model

$\sigma_{k1}$	$\sigma_{k2}$	$\sigma_{\omega 1}$	$\sigma_{\omega 2}$	$\beta_1$	$\beta_2$	$\beta^*$	$\gamma_1$	$\gamma_2$	$\kappa$	$a_1$
0.85	1.0	0.5	0.856	0.075	0.0828	0.09	5/9	0.44	0.41	0.31



environment, we represent the domain using a three-dimensional mesh. This mesh is intricately made up of:

- **Cells** (or Control Volumes): The fundamental units where the integral form of the conservation laws are applied. The solutions—like velocity, pressure, and temperature—are typically stored at the cell centers.
- **Faces**: These are the boundaries of each cell, and they play a critical role as they determine the flux (transfer) of quantities between adjacent cells. Evaluating flux across these faces is pivotal for the conservation properties of the FVM.
- **Vertices**: The corner points of the cells, vertices assist in defining the geometric structure of the mesh and aid in grid generation and adaptation processes.

Given the intricate nature of urban environments, with their myriad structures like buildings and open spaces, creating an accurate grid is paramount. Our meshing strategy ensures a detailed representation of this complexity, capturing the nooks and corners, the highs and lows of the cityscape. This fidelity in geometric representation not only enhances the accuracy of our simulations but also provides invaluable insights into the nuances of fluid flow within urban terrains. Figure 2 shows an example of the mesh that we used in our simulation, which does not have evenly spaced grid cells of consistent size throughout the computational domain. Instead, its resolution varies, allowing for areas of finer detail in regions of interest and coarser resolution elsewhere. This type of mesh is known as nonuniform grid. It begins with a uniform grid and undergoes local refinement in specific areas of interest, such as those near buildings that may induce complex flow patterns.

### 2.3.2 Solution Algorithms

The `pimpleFoam` and `scalarTransportFoam` are used to solve the transient incompressible Navier–Stokes equations (1–2) for the wind flow and the advection–diffusion equation (9) for the dispersion of the pollutants, respectively. The name “pimple” is a hybrid of PISO (Pressure-Implicit with Splitting of Operators) and SIMPLE (Semi-Implicit Method for Pressure Linked Equations). The algorithm combines the advantages of both PISO’s accuracy in transient flows and SIMPLE’s efficiency for steady-state solutions. `scalarTransportFoam` is designed for the passive scalar transport problem. It does not solve for fluid flow; instead, it solves the transport equation for a scalar field, with a given velocity field from the `pimpleFoam`. More details for the solution algorithms can be found in [32].

### 2.3.3 Parallel Computing

To handle the computational demands of large-scale air pollution simulations, our numerical model takes full advantage of high-performance computing (HPC) resources. The simulation code is parallelized using message-passing interface (MPI) techniques, allowing us to distribute the workload across multiple processors and nodes in a supercomputer cluster.

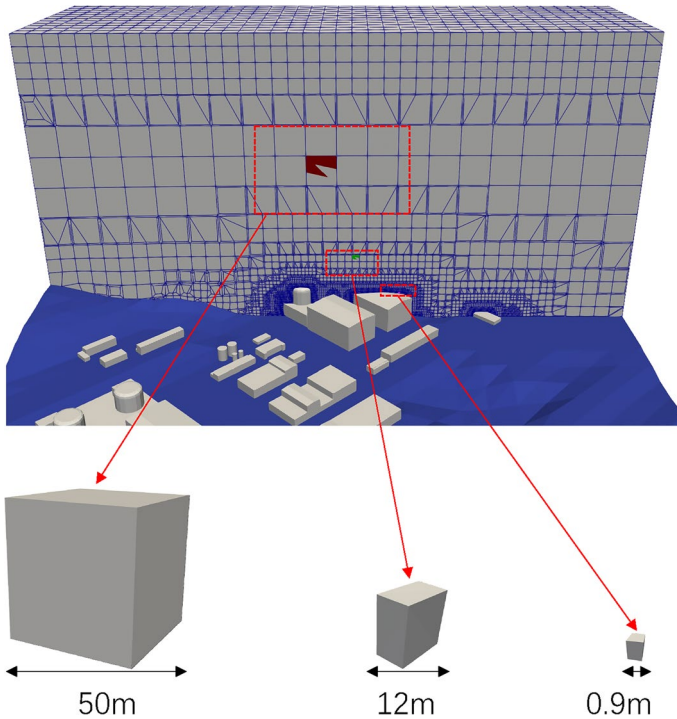


**Fig. 2** An example of the computational mesh. Given the study's primary emphasis on pollutant dispersion near the ground and on building surfaces, these areas have been allocated a more refined mesh to ensure greater precision

Parallelization enhances the scalability of our model, enabling us to simulate complex urban environments at high spatial and temporal resolutions. This approach ensures that our numerical simulations are computationally efficient and capable of handling large-scale scenarios. Figure 3 shows the parallel performance of our simulation on the Tianhe 2A supercomputer at the National Supercomputer Center of Guangzhou China, which shows that the parallel solver scales from 48 to 384 processors and the parallel efficiencies of the solver for Mesh 1 and Mesh 2 are over 87% when the number of processors reaches 384.

In summary, our air pollution distribution model relies on advanced numerical methods and state-of-the-art software tools. These components work in synergy to provide accurate and efficient simulations of pollutant dispersion in urban areas. The combination of numerical discretization, turbulence modeling, and parallel computing empowers our research to explore and understand air quality dynamics in our city comprehensively.

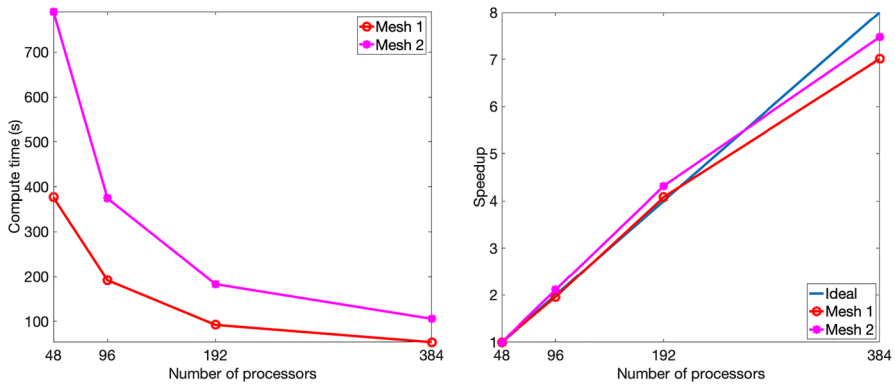


**Fig. 3** Parallel performance metrics of the simulation algorithm: The left graph displays the total simulation time for the initial 20 time steps, while the right graph depicts the parallel speedup. Mesh 1 consists of 22, 668, 403 elements, and Mesh 2 contains 45, 548, 397 elements. The term “Ideal” indicates the ideal speedup scenario, where doubling the number of processors results in the total simulation time being halved

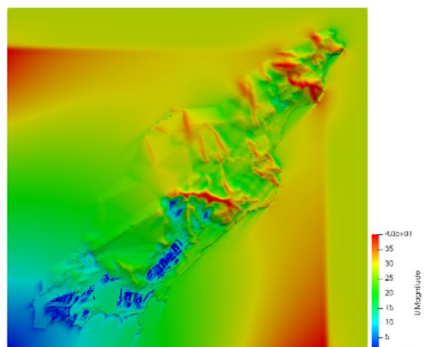
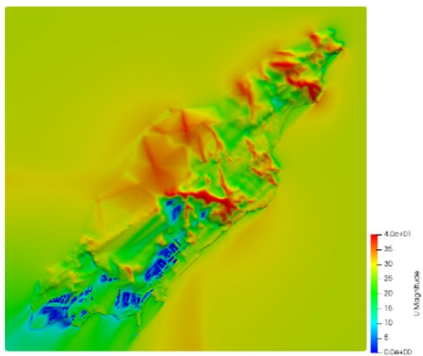
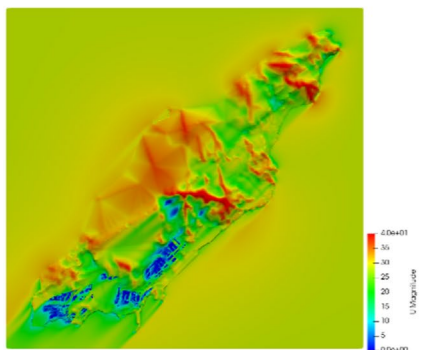
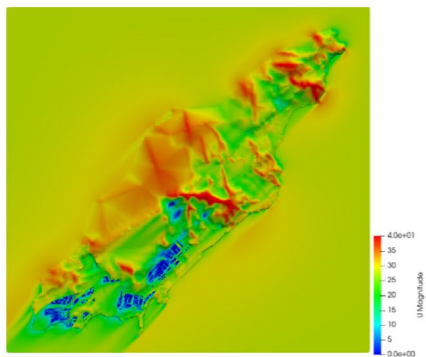
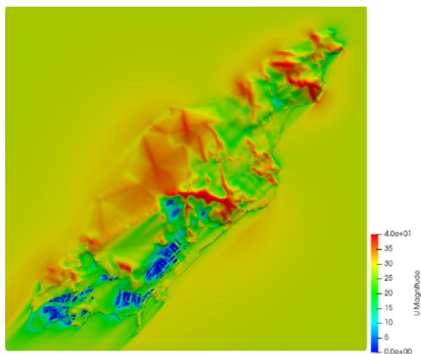
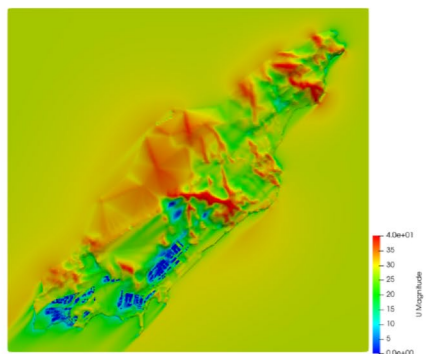
### 3 Results and Discussion

In this section, we offer an in-depth analysis of the results derived from our simulations. Our primary emphasis rests on pivotal parameters: wind field velocity, pressure exerted on building facades, and the dispersion trajectory of pollutants. For the simulation, we employed an 11-level storm field positioned at the top-right, exhibiting a velocity of approximately  $28\text{ m/s}$ . This specific scenario was chosen to closely mirror real-world conditions. We’ll delve into a meticulous exploration of the interplay between these parameters and their collective influence on pollutant behavior and trajectories within our modeled environment.

#### 3.1 Wind Flow Distribution Analysis

Our simulation results, depicted in Fig. 4, illuminate the intricate behavior of wind fields and pollutant dispersion near a nuclear power plant, especially under multifaceted wind conditions. This study prioritizes the understanding of how wind turbulence and thermal stability influence the dispersion and movement of pollutants within this context.

In Fig. 4a, the simulation’s early phase reveals some wind velocity instability, creating pockets of significantly high wind speeds. This initial turbulence is likely due to the flow field’s inherently chaotic nature at the simulation’s onset. However, over a span of 600 s, the wind field shows a stabilizing trend, eventually aligning with the targeted inlet velocity of  $28\text{ m/s}$ . Figure 4d visually underscores this stabilization, affirming its alignment with the preset conditions. These observations are instrumental in discerning how varying wind patterns influence

(a) At the time  $T = 50$  seconds(b) At the time  $T = 200$  seconds(c) At the time  $T = 400$  seconds(d) At the time  $T = 600$  seconds(e) At the time  $T = 800$  seconds(f) At the time  $T = 1000$  seconds

**Fig. 4** The visual representation illustrates the spatiotemporal evolution of wind field dynamics, given initial boundary conditions with a velocity of 28 m/s. A color map, transitioning from Blue (0 m/s) to Red (40 m/s), depicts the velocity magnitudes. The depicted flow patterns capture intricate phenomena, including vortices, turbulence, and eddies, all of which significantly influence the dispersion and movement of pollutants in urban settings

pollutant dispersion near the nuclear facility, offering vital data for safety and environmental evaluations.

Moreover, our simulations highlight the profound influence of intricate terrains on wind fields and pollutant paths. For instance, mountainous gradients modify the wind field, propelling the wind to ascend along slopes and leading to high-velocity zones—red areas indicate speeds of about 35–40 m/s. Conversely, on the mountain's leeward side, obstruction-induced decelerations result in wind speeds of roughly 15–20 m/s, as indicated by the light-green areas. Furthermore, structures like buildings further impede wind flow, creating regions, shown in blue, where velocities dwindle to a mere 5–10 m/s.

In summation, these simulation insights afford a holistic view of wind and pollutant dynamics near a hypothetical nuclear power plant amidst intricate wind scenarios. By leveraging sophisticated tools like CFD, we can precisely anticipate how pollutants disperse, factoring in terrain nuances and wind variability. These insights hold paramount importance for enhancing nuclear plant safety protocols, emergency readiness, and mitigating potential environmental and health impacts.

### 3.2 Velocity at the Outlet Boundary

Velocity Distribution Analysis at the Bottom Outlet: Fig. 5 offers an examination of the wind field's behavior across distinct time intervals, specifically charting the transition from the right to the left side of the bottom outlet. The figure illustrates that during the 50 and 200-second timestamps, the velocity distribution, represented by the red and yellow lines, is notably volatile, with differences nearing 40 and 16, respectively. Such fluctuations can be ascribed to the turbulent flow behaviors typical of the simulation's outset.

Yet, as time advances, a more consistent velocity distribution emerges, evident from the green and brown lines representing the 400 and 600-second intervals. Remarkably, the velocity remains consistent across the 600, 800, and 1000-s marks, implying a stabilization of the wind field post the 600-s point. This stabilization resonates with the average wind field velocity lingering around 28–30 m/s, mirroring the pre-set inlet wind speed.

For a more precise confirmation of this wind field stabilization, we contrasted the average velocities between the 400 and 600-second intervals. The result, with a ratio of  $28.7126 \div 28.7987 \approx 0.997$ , attests to a negligible deviation, underscoring the wind field's post-600-s stabilization.

Importantly, such stabilization is paramount for effectively forecasting pollutant dispersion. Leveraging CFD techniques to model wind field behavior over varied timeframes allows for enhanced, dependable predictions on pollutant transport and dispersion. This in turn bolsters our capabilities in environmental risk mitigation and public health protection.

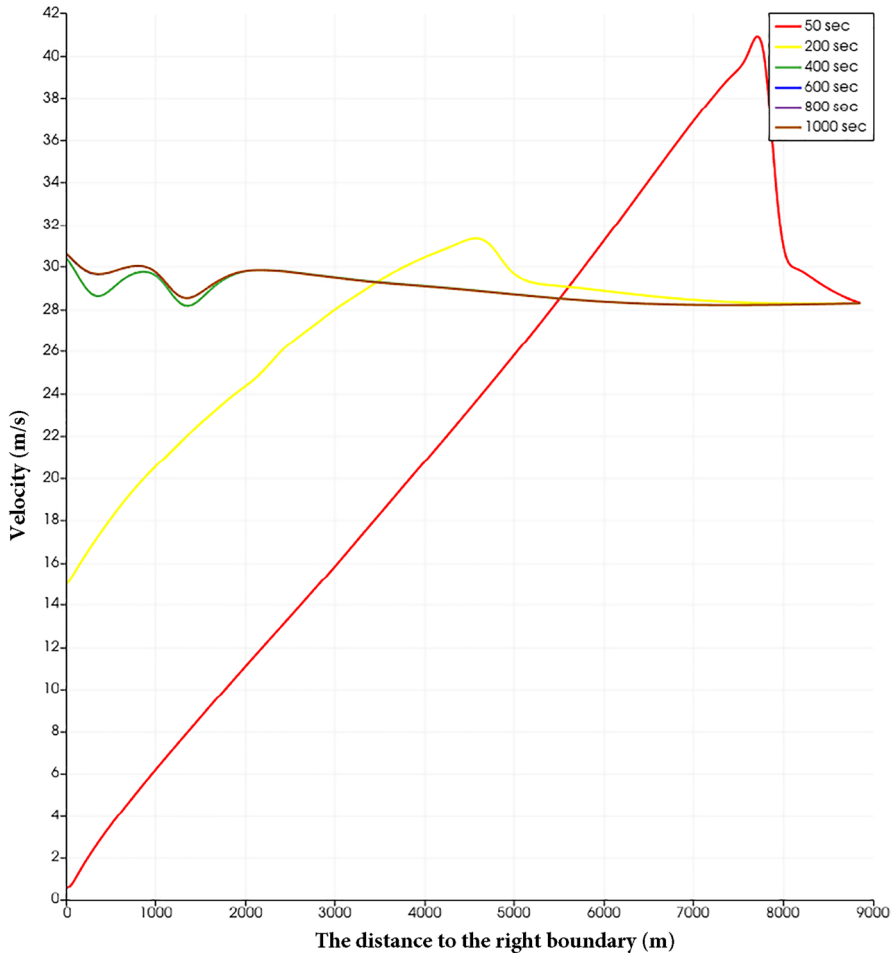
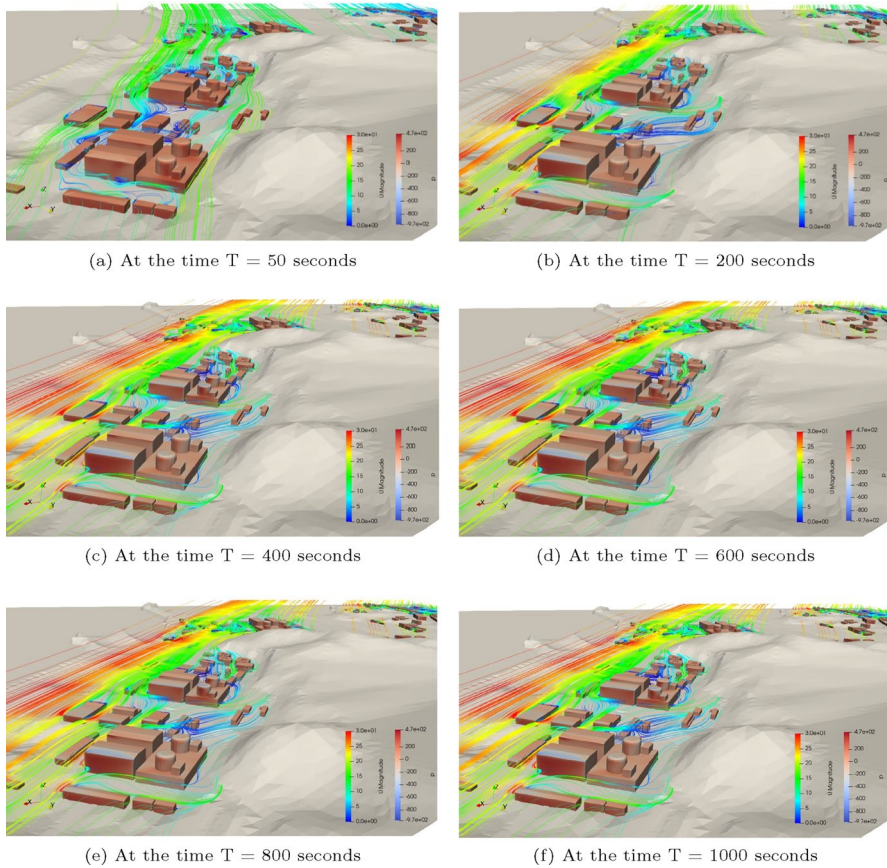


Fig. 5 Variations in wind speed at the outlet boundary over time

### 3.3 Pressure on the surface of buildings

The distribution of pressure across a building’s surface profoundly impacts its structural integrity and its ability to withstand wind-induced damages. Our study, visually represented in Fig. 6, reveals the dynamics of this pressure distribution. The windward side of the building, directly exposed to the wind, experiences a notable surge in pressure, with intensities peaking at 470 Pa in deep-red highlighted areas. The building’s surface area significantly influences these pressure metrics, as larger buildings tend to register higher pressures, manifested by the more intense red regions.

Another intriguing observation is the wind’s interaction with the building. As it collides with the structure, the wind is inclined to ascend along the facade.



**Fig. 6** Visualization of pressure distribution on the surfaces of buildings at distinct time intervals. In each image, color bars represent both velocity and pressure values. Velocity ranges from Blue (0 m/s) to Red (40 m/s), while pressure spans from Blue (−970 Pa) to Red (470 Pa)

This creates a localized negative pressure near the eaves, signified by the milky white or blue regions in the pressure diagram, with pressure levels plummeting to  $-400$  Pa.

The leeward side of the building (opposite the windward side) demonstrates the effects of wind deflection. Here, pressure diminishes due to the barrier provided by the building. Interestingly, the roof's average pressure approximates zero, indicating its relative isolation from direct wind exposure.

In essence, these CFD simulations furnish essential details about pressure nuances on building exteriors. Such insights hold paramount significance for architects and construction professionals, guiding them towards designs that optimize a building's resistance to wind-related adversities.

### 3.4 Pollutants Dispersion

This study delves into simulating the spread of radioactive aerosols, particles (solid or liquid) imbued with radioactive isotopes, in the atmosphere. Such aerosols originate when atmospheric particles absorb radioactive fission products. Their diffusion range, symbolizing the spread of the pollutant, is paramount for understanding environmental pollution dynamics. For clarity in visualization, pollutant concentrations are denoted in ppm (parts per million), as depicted by the color bar in Fig. 7. The more intense the pollutant concentration, the redder the shade; conversely, lower concentrations are bluer. Pollutant aggregation levels are depicted using dot densities, where denser clusters signify higher concentrations.

Figure 1b earmarks the pollutant source with a red “3”. Naturally, this location registers the deepest red shade, signifying peak concentration. Superimposed streamlines outline wind patterns, flowing from the top-right to bottom-left, steering pollutants in its wake. The most distant areas from the source exhibit the lightest shades and sparsest dots.

The interplay between wind and topographical features is evident. Mountains, acting as barriers, cause wind speeds to drop to 10–20 m/s at the 50-s mark (as

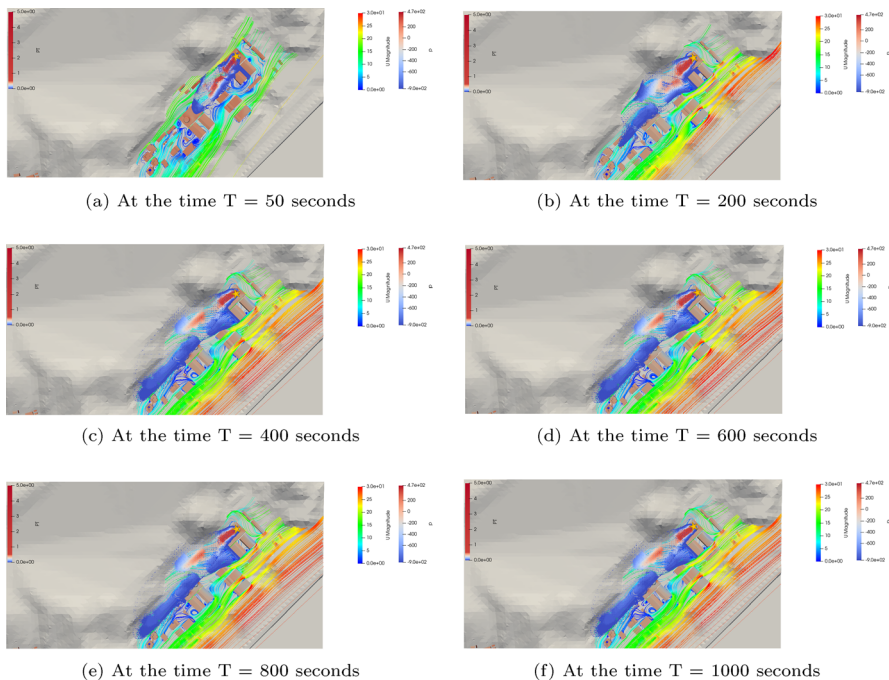


**Fig. 7** The spatiotemporal evolution of pollutant dispersion trajectories under an initial velocity of 28m/s. The images display the concentration distribution of pollutants across different timestamps, complemented by three color bars representing PT, velocity, and pressure values. Specifically, PT values span from Blue (0 ppm) to Red (5 ppm), velocity from Blue (0 m/s) to Red (30m/s), and pressure from Blue (-900 Pa) to Red (470 Pa)



green zones in the figure show). This deceleration is contrasted with the original inlet speed of 28 m/s. Upon stabilization post 600 s, wind speeds in open areas hover around 25–30 m/s (orange zones). However, wind speeds dip to 15 m/s behind edifices due to obstruction, while corners retain speeds of 25–30 m/s.

For buildings situated in semi-open locales, the windward side experiences heightened pressure, whereas the leeward and lateral aspects, alongside eaves, undergo a drop owing to airflow dynamics. This disparity births localized vortex flows, visible as deep blue vortexes with speeds ranging 0–5 m/s. The study also discerned the Karman vortex street phenomenon. Pressure variances at eaves compel pollutants to ascend along facades, distancing them from the ground. Such revelations underscore the intricate interdependencies between flow dynamics and urban topographies in predicting pollutant trajectories.

## 4 Conclusion

This study embarked on an ambitious journey to comprehend the multifaceted interactions between wind, urban topography, and pollutant dispersion, particularly in the vicinity of a nuclear power plant. The conclusions drawn from this research are manifold:

- **Topographical Influence:** The results underscored the salient role of topography in modifying airflow and pollutant trajectories. Natural structures, such as mountains, can significantly alter wind speeds, while man-made structures, especially buildings, can create pockets of varied wind velocities, leading to complex pollutant distributions.
- **Numerical Simulation:** The strength of computational fluid dynamics was profoundly exhibited through this research. Our methodologies, encompassing the finite volume methods and the employment of state-of-the-art software tools like `pimpleFoam` and `scalarTransportFoam`, delivered accurate and detailed simulations. These techniques provided nuanced insights into pressure distributions on buildings and wind field stabilization over time.
- **Pressure Dynamics:** The study shed light on pressure dynamics on building facades. Wind-induced pressure on a building's windward side can peak significantly, potentially posing structural challenges. Furthermore, the negative pressure observed near the eaves of buildings can influence pollutant dynamics, making them rise along building facades, a phenomenon that has implications for the design and positioning of ventilation systems and structural integrity.
- **Pollutant Dispersion:** The dispersion of radioactive aerosols was meticulously charted. The patterns unveiled the role of airflow in directing pollutants, with distant areas from the source registering minimal concentrations. Yet, the influence of local topographical features and structures created complex dispersion patterns, including localized vortex flows and the Karman vortex street phenomenon.
- **Relevance to Real-world Scenarios:** The simulation's alignment with real-world wind speeds and conditions amplified the practical relevance of the study.

Such findings have paramount importance for nuclear safety, urban planning, and emergency response. Accurate predictions of pollutant spread can aid in developing timely evacuation plans, implementing safety protocols, and informing the public about potential risks.

- **Scalability & Efficiency:** The effective harnessing of high-performance computing resources via parallel computing ensured the scalability and efficiency of our simulations. This approach permitted us to handle large-scale scenarios, further reinforcing the robustness and practical applicability of our findings.

In wrapping up, the significance of this study lies not only in its scientific rigor but also in its societal implications. Through an amalgamation of advanced numerical methods, topographical insights, and real-world relevance, this research serves as a cornerstone for ensuring the safety and well-being of communities living in proximity to nuclear plants and other potential pollutant sources. The insights gleaned have set the foundation for future research, policy recommendations, and enhanced urban and nuclear facility design.

**Author Contributions** The authors declare that the study was realized in collaboration with equal responsibility. All authors read and approved the final manuscript.

**Funding** This research was funded by NSFC (No. 62161160312 and 12001520) and Shenzhen basic research fund under RCYX20200714114735074.

**Availability of Data and Materials** The data that support the findings of this study are available from the corresponding author, CR, upon reasonable request.

## Declarations

**Conflict of Interest** The authors declare there is no conflicts of interest.

**Ethics approval and consent to participate** Not applicable.

**Consent for Publication** Not applicable.

**Open Access** This article is licensed under a Creative Commons Attribution 4.0 International License, which permits use, sharing, adaptation, distribution and reproduction in any medium or format, as long as you give appropriate credit to the original author(s) and the source, provide a link to the Creative Commons licence, and indicate if changes were made. The images or other third party material in this article are included in the article's Creative Commons licence, unless indicated otherwise in a credit line to the material. If material is not included in the article's Creative Commons licence and your intended use is not permitted by statutory regulation or exceeds the permitted use, you will need to obtain permission directly from the copyright holder. To view a copy of this licence, visit <http://creativecommons.org/licenses/by/4.0/>.

## References

1. Tominaga, Y., Stathopoulos, T.: Cfd simulation of near-field pollutant dispersion in the urban environment: a review of current modeling techniques. *Atmos. Environ.* **79**, 716–730 (2013)
2. Yang, S., Wang, L.L., Stathopoulos, T., Marey, A.M.: Urban microclimate and its impact on built environment—a review. *Build. Environ.* **238**, 110334 (2023)

3. Wen, H., Malki-Epshtein, L.: A parametric study of the effect of roof height and morphology on air pollution dispersion in street canyons. *J. Wind Eng. Ind. Aerodyn.* **175**, 328–341 (2018)
4. Akhter, M.N., Ali, M.E., Rahman, M.M., Hossain, M.N., Molla, M.M.: Simulation of air pollution dispersion in Dhaka city street canyon. *AIP Adv.* **11**(6), 065022 (2021)
5. Ali, M.E., Hasan, M.F., Siddiqui, S., Molla, M.M., Akhter, M.N.: FVM-RANS modeling of air pollutants dispersion and traffic emission in Dhaka city on a suburb scale. *Sustainability* **15**(1), 673 (2023)
6. Zheng, X., Montazeri, H., Blocken, B.: Large-eddy simulation of pollutant dispersion in generic urban street canyons: Guidelines for domain size. *J. Wind Eng. Ind. Aerodyn.* **211**, 104527 (2021)
7. Letzel, M.O., Helmke, C., Ng, E., An, X., Lai, A., Raasch, S.: LES case study on pedestrian level ventilation in two neighbourhoods in Hong Kong. *Meteorol. Z.* **21**(6), 575–589 (2012)
8. Janssen, W., Blocken, B., Hooff, T.: Pedestrian wind comfort around buildings: comparison of wind comfort criteria based on whole-flow field data for a complex case study. *Build. Environ.* **59**, 547–562 (2013)
9. Montazeri, H., Blocken, B., Janssen, W., Hooff, T.: CFD evaluation of new second-skin facade concept for wind comfort on building balconies: Case study for the Park Tower in Antwerp. *Build. Environ.* **68**, 179–192 (2013)
10. Onodera, N., Aoki, T., Shimokawabe, T., Kobayashi, H.: Large-scale LES wind simulation using lattice Boltzmann method for a 10 km× 10 km area in metropolitan Tokyo. *Tsubame ESJ* **9**(2), 1–8 (2013)
11. Shi, X., Zhu, Y., Duan, J., Shao, R., Wang, J.: Assessment of pedestrian wind environment in urban planning design. *Landsc. Urban Plan.* **140**, 17–28 (2015)
12. Ikeda, R., Kusaka, H., Iizuka, S., Boku, T.: Development of urban meteorological model for thermal environment at city scale. In: *Proceedings of the General Meeting of the Association of Japanese Geographers Annual Meeting of the Association of Japanese Geographers, Autumn 2014*, p. 61 The Association of Japanese Geographers (2014)
13. Zheng, C., Li, Y., Wu, Y.: Pedestrian-level wind environment on outdoor platforms of a thousand-meter-scale megatall building: Sub-configuration experiment and wind comfort assessment. *Build. Environ.* **106**, 313–326 (2016)
14. Jacob, J., Sagaut, P.: Wind comfort assessment by means of large eddy simulation with lattice Boltzmann method in full scale city area. *Build. Environ.* **139**, 110–124 (2018)
15. Sousa, J., Górlé, C.: Computational urban flow predictions with Bayesian inference: Validation with field data. *Build. Environ.* **154**, 13–22 (2019)
16. Liu, Y., Liu, C.-H., Brasseur, G.P., Chao, C.Y.H.: Empirical mode decomposition of the atmospheric flows and pollutant transport over real urban morphology. *Environ. Pollut.* **331**, 121858 (2023)
17. Fiates, J., Vianna, S.S.: Numerical modelling of gas dispersion using openfoam. *Process Saf. Environ. Prot.* **104**, 277–293 (2016)
18. Zhang, Y., Kwok, K.C., Liu, X.-P., Niu, J.-L.: Characteristics of air pollutant dispersion around a high-rise building. *Environ. Pollut.* **204**, 280–288 (2015)
19. Liu, Y., Cui, G., Wang, Z., Zhang, Z.: Large eddy simulation of wind field and pollutant dispersion in downtown Macao. *Atmos. Environ.* **45**(17), 2849–2859 (2011)
20. Gousseau, P., Blocken, B., Stathopoulos, T., Heijst, G.F.: Near-field pollutant dispersion in an actual urban area: analysis of the mass transport mechanism by high-resolution large eddy simulations. *Comput. Fluids* **114**, 151–162 (2015)
21. Liu, H.: A global uniqueness for formally determined inverse electromagnetic obstacle scattering. *Inverse Prob.* **24**(3), 035018 (2008)
22. Li, J., Liu, H., Wang, Q.: Enhanced multilevel linear sampling methods for inverse scattering problems. *J. Comput. Phys.* **257**, 554–571 (2014)
23. Li, J., Li, P., Liu, H., Liu, X.: Recovering multiscale buried anomalies in a two-layered medium. *Inverse Prob.* **31**(10), 105006 (2015)
24. Li, H., Li, J., Liu, H.: On quasi-static cloaking due to anomalous localized resonance in  $\mathbb{R}^3$ . *SIAM J. Appl. Math.* **75**(3), 1245–1260 (2015)
25. Blasten, E., Liu, H.: Recovering piecewise constant refractive indices by a single far-field pattern. *Inverse Prob.* **36**(8), 085005 (2020)
26. Yin, Y., Yin, W., Meng, P., Liu, H.: On a hybrid approach for recovering multiple obstacles. *Commun. Comput. Phys.* **31**(3), 869–892 (2022)

27. Chen, X., Lin, X., Zhang, L., Skalomenos, K.A.: Method for rapidly generating urban damage scenarios under non-uniform ground motion input based on matching algorithms and time history analyses. *Soil Dyn. Earthq. Eng.* **152**, 107055 (2022)
28. Cheng, Z., Chen, R., Sun, Z.: A parallel numerical simulation method for the aerodynamics of rotor unmanned aerial vehicles based on unstructured sliding meshes. *J. Integr. Technol.* **6**(3), 82–91 (2017)
29. Yan, Z., Chen, R., Zhao, Y., Cai, X.-C.: A scalable numerical method for simulating the external flows around cars. *J. Integr. Technol.* **4**(1), 25–36 (2015)
30. Menter, F.R.: Two-equation eddy-viscosity turbulence models for engineering applications. *AIAA J.* **32**(8), 1598–160500011452 (1994)
31. Toparlar, Y., Blocken, B., Maiheu, B., Van Heijst, G.: A review on the cfd analysis of urban microclimate. *Renew. Sustain. Energy Rev.* **80**, 1613–164013640321 (2017)
32. Greenshields, C., Weller, H.: Notes on Computational Fluid Dynamics: General Principles. CFD Direct Ltd, Reading (2022)